Reaction Kinetics, Mechanisms and Catalysis (2023) 136:287–309
https://doi.org/10.1007/s11144-022-02334-3

Production of levulinic acid from glucose using nickel phosphate-silica catalyst

Qodria Utami Putri[1,2] · Hasanudin Hasanudin[2,3] · Wan Ryan Asri[1,2] · Ady Mara[2,3] · Roni Maryana[4] · Saharman Gea[5] · Karna Wijaya[6]

Received: 18 September 2022 / Accepted: 13 December 2022 / Published online: 18 December 2022

Abstract

A combination of nickel-silica and nickel phosphate is hypothesized to provide a synergistic effect on catalytic processes of LA production from glucose. This research aims to produce LA from glucose by employing nickel phosphate-silica catalysts. The effect of different phosphate catalyst precursors on the yield of LA was investigated. Catalysts were assessed by using FT-IR, SEM–EDX, XRD, and N_2 adsorption–desorption isotherms. Acidity analysis for the catalysts was performed by the gravimetric method. The product of levulinic acid was examined by HPLC. The study exhibited that the incorporation of phosphate ions into nickel-silica increased the acidity of the catalyst and inherently provided an increase in LA yield. It was found that the hydrogen atoms number from different phosphate precursors showed a positive correlation to the increase in LA yield as well. $Ni(H_2PO_4)_2$–SiO_2 catalyst had the highest activity compared to the others catalysts on LA formation, whereas $Ni_3(PO_4)_2$–SiO_2 dominantly promoted formic acid formation. Further optimization by RSM-CCD showed that the optimum condition was achieved at a temperature of 113.20 °C, a reaction time of 120 min, and a catalyst weight of 0.4573 g with an LA yield of 40.89%. The quadratic model as derived from RSM-CCD demonstrated good accuracy in estimating the output parameter. This catalyst was still active at 5 consecutive runs with a slight decrease toward LA formation.

Keywords Nickel-silica · Nickel phosphate-silica · Levulinic acid production · RSM-CCD

✉ Hasanudin Hasanudin
hasanudin@mipa.unsri.ac.id

Extended author information available on the last page of the article

Introduction

The petrochemical industry is an industry that produces organic compounds derived from oil and natural gas. With the development of the petrochemical industry, the use of fossil fuels increases whilst the availability of fossil fuels decreases over time. Thus, finding other alternative precursors to fossil fuels is necessary [1–3]. To remedy such a situation, platform chemicals can be employed as a potential replacement for fossil fuels in the industries that process them, especially the petrochemical industry [4]. Levulinic acid (LA) is a platform chemical containing five carbon atoms of carboxylic acid, and ketone groups may be used as building blocks that has good reactivity [5, 6]. LA has now become a major platform chemical in biorefinery used for various applications [7, 8], and industries such as pharmaceuticals, textiles, solvents, food flavoring agents, and dyes [9].

Generally, LA can be synthesized by dehydrating and rehydrating lignocellulosic biomass (cellulose, hemicellulose, and starch) [10] or hexose sugars (glucose, fructose, and galactose) [11]. The glucose dehydration produces 5-Hydroxymethylfurfural (5-HMF), and prolonged rehydration produces levulinic acid and formic acid as by-products [12]. The dehydration and rehydration processes usually use homogeneous catalysts, such as orthophosphoric, hydrochloric, and sulfuric acid as well. However, these strong acid catalysts are non-environmental friendly, difficult to be recycled and separated, and may cause corrosion [13, 14]. Therefore, heterogeneous catalysts are more preferred and widely used to tackle the shortcomings of homogeneous catalysts [15].

In the production of LA, heterogeneous catalysts of many types have previously been used, such as $SO_4^{2-}/TiO_2–Al_2O_3–SnO_2$ [16], metal–organic framework (MOF) [14], MFI-type zeolites [17], acid clay, and ion exchange resin [18], Al–Zr mixed oxides [19], and metal(IV) phosphate [20]. Likewise, nickel-silica is a catalyst with good stability that is often used in catalytic processes [21]. The catalyst has sufficient strong acid and active metal sites [22], in addition to large surface areas and strong nickel-silica interactions [23]. Meanwhile, nickel phosphate is a metal-phosphate catalyst of strong interest for its unique physical and chemical properties [24]. This catalyst has large surface areas, as well as good acidity and stability [25]. The presence of phosphate groups in the metals provides advantageous properties in catalytic processes as it provides medium-strong Lewis acid (metal site) and Brønsted acid (protonated phosphate group) sites in charge of the high catalytic activity of the catalyst [26, 27].

Combining nickel-silica and nickel phosphate is theorized to provide a synergistic effect on catalytic processes due to the similarity in acidity and stability of the two catalysts. Many studies have reported the use of nickel phosphate catalysts use in various applications [28–31]. However, reports nor studies have yet been made on the production of LA from glucose catalyzed by nickel phosphate-silica catalyst. The strength and acidity of a catalyst are influenced by the type of phosphate ion and the number of hydrogen atoms present in the precursor. These two conditions directly affect the performance of a catalyst during catalysis [32].

This research explores two primary aspects, starting with the fabrication of nickel phosphate silica using different phosphate precursors (ammonium dihydrogen phosphate, diammonium hydrogen phosphate, and tributyl phosphate) and evaluating their catalytic activity in the production of LA from glucose. The catalyst with the best properties and highest yield would be further investigated for reaction temperature, reaction time, and catalyst weight effects on LA yield through the design of experiment (DoE) using response surface methodology (RSM) with rotatable central composite design (RCCD). In this regard, the quadratic polynomial equation was utilized as a model and subsequently examined using ANOVA (95% confidence level). The 3D surface and 2D contour model graphs were plotted, and the interaction of variables on the response was thoroughly studied. The catalysts from the different precursors were assessed using FT-IR, SEM–EDX, XRD powder, and N_2 adsorption–desorption isotherms. Acidity analysis for the catalysts was performed by using the gravimetric method.

Experimental

Materials

The materials employed in this study were silver nitrate, ammonium dihydrogen phosphate, diammonium hydrogen phosphate, tributyl phosphate, absolute ethanol, 25% ammonia solution, glucose, and nickel(II) nitrate hexahydrate. All chemicals were analytical grade obtained from Merck.

Preparation of silica

The SiO_2 powder was prepared by firstly mixing 50 mL of absolute ethanol with 5 mL distilled water and subsequently stirred for 15 min. Into the mixture, 5.6 mL tetraethyl orthosilicate (TEOS) and 1 mL 28% ammonia solution was added and stirred using a magnetic stirrer for 3 h at ambient temperature. The gel formed was heated for 24 h at 85 °C. The dried powder was then sieved using a 200-mesh sieve.

Synthesis of nickel-silica

4.5 g of silica powder was dispersed in 100 mL of 0.02 M of nickel(II) nitrate hexahydrate solution and stirred with magnetic stirrer for 3 h at room temperature. The solution was subsequently dried in the oven for 24 h at 105 °C. The dried powder was calcined at 700 °C for 4 h. The Ni-SiO_2 catalyst was then sieved using a 200-mesh sieve [21].

Synthesis of nickel phosphate-silica

A series of nickel phosphate-silica catalysts $Ni_3(PO_4)_2$–SiO_2, $NiHPO_4$–SiO_2, and $Ni(H_2PO_4)_2$–SiO_2 were prepared by using different phosphate precursors [33]. $Ni_3(PO_4)_2$-SiO_2 catalyst was synthesized from 0.002 mol of nickel(II) nitrate hexahydrate mixed with 0.0013 mol of tributyl phosphate and dissolved in distilled water in a 100 mL volumetric flask. After, 4.5 g of silica powder was then dispersed in the solution and stirred for 1 h. The mixture was then heated at 100 °C for 1 day followed by calcination at 700 °C for 4 h. The catalyst was then sieved using a 200-mesh sieve. Meanwhile, $NiHPO_4$-SiO_2 and $Ni(H_2PO_4)_2$–SiO_2 catalysts were synthesized from 0.002 mol of nickel(II) nitrate hexahydrate mixed with 0.002 mol of diammonium hydrogen phosphate and 0.004 mol of ammonium dihydrogen phosphate, respectively. The solutions were then dissolved in distilled water in a 100 mL volumetric flask. Subsequently, 4.5 g of silica powder was then dispersed in each of the solutions and stirred for 1 h. Subsequently, the mixtures were heated at 120 °C for 24 h. The dried powder was then sieved using a 200-mesh sieve.

Production of levulinic acid

Glucose was first dried at 105 °C for 3 h to achieve a constant weight. 2 g of the glucose was then added into 50 mL distilled water, followed by 0.5 g catalyst [12]. Next, the mixture was refluxed at 120 °C for 3 h with stirring. The refluxed solution was then centrifuged at 5000 rpm for 5 min at ambient temperature and the supernatant was analyzed using HPLC (Zorbax SB-C18 column, UV detector (268 nm) with a flow rate 1 mL/min using H_2SO_4 (0.0005 M) solution as the mobile phase at 30 °C). The glucose conversion (C_x), LA and formic acid yield (Y_x) as well as selectivity (S_x) were calculated according to the Eqs. 1–3 as follows:

$$C_X = \left(\frac{\text{reacted glocuse mole}}{\text{intial glocuse mole}}\right) \times 100\% \tag{1}$$

$$Y_X = \left(\frac{\text{LA or FA product mole}}{\text{Glucose initial mole}}\right) \times 100\% \tag{2}$$

$$S_X = \left(\frac{\text{LA or FA product mole}}{\text{reacted glucose mole}}\right) \times 100\% \tag{3}$$

In order to evaluate the catalyst reusability, the spent catalyst was regenerated through the washing process using water followed by heat treatment. The spent catalysts were dried at 100 °C for 24 h and calcined at 700 °C for 4 h to discharge the humin absorbed on the catalyst

Catalyst characterization

X-ray diffraction (XRD) powder was performed using Rigaku Mini Flex 600 with a Cu K_α radiation. The functional groups of catalysts were evaluated using Shimadzu FTIR 8201 (spectra were scanned from 400 to 4000 cm^{-1}). Acidity analysis followed the gravimetric method with pyridine gas, as reported by the previous study [34]. Scanning electron microscope-energy dispersive X-ray Spectroscopy (SEM–EDX) was performed using JEOL-JSM 6510 LA with 20 kV accelerating voltage. N_2 physisorption isotherms at 77.3 K measured using Quantachrome NOVA.

Experimental design

RSM-CCD were employed to provide the design of experiments (DoE) with the assistance of Design Expert Software 12. RSM requires a minimum number of experiments and is very useful in increasing the accuracy of the design process [35]. RSM-CCD is one of the essential tools for data modeling, collection, and optimization to determine how several input variables affect the responses [36, 37]. In general, CCD runs involved the sum of factorial (2^n), axial (2n), and central (n_c) points [38]. In this study, three input variables; (n = 3) temperature (A), reaction time (B), and catalyst weight (C), with LA yield (Y) as the output variable were investigated. Consequently, 8 factorial, 6 axial, and 6 central runs (20 total experiments) were selected in this study. The center point was repeated six times to calculate the error and standard deviation [39]. Each variable was coded ± 1, 0, and ± α (± 1.682) for the factorial, center, and axial points, respectively [40]. The ranges of variables studied are shown in Table 1.

Analysis of variance was employed to examine the experimental result as well as the model. The statistical significance was assessed using F-test and P-value (95% confidence level) [41]. Analysis of regression was conducted to investigate the Y response function [42], as formulated in Eq. 4 as follows:

$$Y = \beta_o + \sum_{i=1}^{k} \beta_i X_i + \sum_{i=1}^{k} \beta_{ii} X_i^2 + \sum_{i=1}^{k-1} \sum_{j=2}^{k} \beta_{ij} X_i X_j + \varepsilon \quad (4)$$

Here i and j are linear and quadratic coefficients, respectively, βo was the coefficient of regression, and k was the number of independent variables studied. According to Behera et al. [43], CCD was utilized for the quadratic effect due to an individual second-order effect could not be separately estimated by 2^n factorial designs.

Table 1 Independent variables used for CCD in the production of LA

Variables	Unit	Levels				
		− 1.682	− 1	0	1	+ 1.682
Temperature (A)	°C	103.18	110	120	130	136.82
Reaction time (B)	min	79.09	120	180	240	280.91
Catalyst weight (C)	g	0.25	0.35	0.5	0.65	0.75

The RSM method was reasonable to fit a typical surface of quadratic and it helped optimizing the parameters of process.

Results and discussion

Catalyst characterizations

The characterization using XRD was employed to determine the structural properties of nickel phosphate-silica catalysts. The diffractogram in Fig. 1a shows that Ni-SiO_2 catalyst had a wide peak at 2θ of 22°, corresponding to amorphous silica [44]. Sharp crystalline peaks were observed in Ni-SiO_2 catalyst at 2θ of 37.2°, 43.2°, and 62.7°. According to Mallesham et al. [22], these peaks represent NiO compounds with a face-centered cubic Ni structure. The $Ni_3(PO_4)_2$–SiO_2 catalyst as shown in Fig. 1b, had sharp peaks at 2θ of 37.1°, 43.25°, and 75.5°, indicating crystalline phases that could be attributed to the calcination of nickel phosphate [25]. This finding was in line with JCPDS No. 00-035-0987. Meanwhile, the $NiHPO_4$-SiO_2 catalyst, as shown in Fig. 1c, revealed diffraction peaks at 2θ of 8.96° and 35.52°, which represented the $NiHPO_4$ compound [33], whereas the broad peak at 2θ of 22.43° corresponded to the silica compound [45]. Furthermore, $Ni(H_2PO_4)_2$-SiO_2 diffractogram in Fig. 1d showed sharp peaks at 2θ of 17.2°, 24.04°, and 29.30°, confirming the presence of amorphous nickel phosphate [28], and silica compound (JCPDS No. 76-0933).

The spectra of Ni–SiO_2 catalyst in Fig. 2a revealed an absorption peak band at ~ 1051 cm^{-1} and 822 cm^{-1} indicating stretching vibration of Ni–O bond [46], and Si–O-Si bonding vibration, respectively, confirming the interaction between

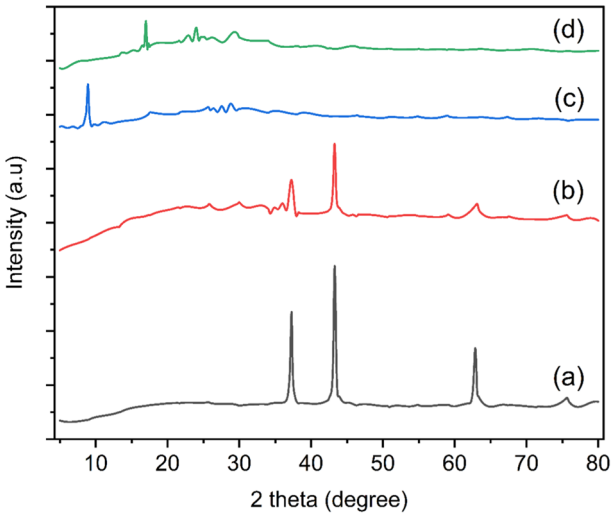

Fig. 1 XRD diffractograms of (a) Ni–SiO_2, (b) $Ni_3(PO_4)_2$–SiO_2, (c) $NiHPO_4$–SiO_2 and (d) $Ni(H_2PO_4)$–SiO_2 catalysts

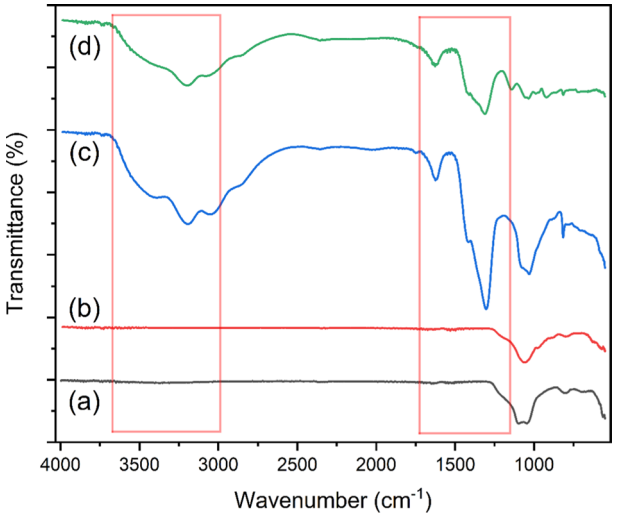

Fig. 2 FTIR spectra of (a) Ni–SiO_2, (b) $Ni_3(PO_4)_2$–SiO_2, (c) $NiHPO_4$–SiO_2 and (d) $Ni(H_2PO_4)$–SiO_2 catalyst

silica and Ni–O [47]. These peaks were also observed in all the other catalysts. Subsequently, a weak absorption at 721 cm^{-1} as in Fig. 2b of $Ni_3(PO_4)_2$–SiO_2 catalyst corresponded to the vibration of P–O bonding [48], and the absorptions at ~ 936 cm^{-1} and 994 cm^{-1} represent the stretching vibration of PO_4^{-3} tetrahedral structure [49]. These findings were consistent with the previous reports [50]. For the $NiHPO_4$-SiO_2 catalyst as shown in Fig. 2c, the spectra revealed a wide absorption peak at 3205 cm^{-1}, which is associated with HPO_4 vibration [51].

The absorption bands at 3052 and 1633 cm^{-1} indicated the stretching vibration of the hydroxyl group and the bending mode of water molecules that were physically adsorbed onto the catalyst surface [49, 50]. In the meantime, the weak absorption peak at 2358 cm^{-1} indicated the P–O–H bonding vibration [52]. This phosphate absorption was consistently reported by Liu et al. [30] previously. The same absorption bands were also observed in $Ni(H_2PO_4)$–SiO_2 (Fig. 2d). However, the P–O–H bonding vibration was not observed in Ni–SiO_2 and $Ni_3(PO_4)_2$–SiO_2 catalysts confirming that they did not have hydrogen bonding interaction from the phosphate ion.

Micrographs from the surface morphology analysis of the catalysts using SEM are shown in Fig. 3. Ni–SiO_2 catalyst in Fig. 3a shows a nearly uniform size and shape of pores, indicating good interaction between nickel and silica [53]. Meanwhile, $Ni_3(PO_4)_2$–SiO_2 catalyst in Fig. 3b showed nickel phosphate aggregations that were evenly distributed on the surface with a tight arrangement as a result of the calcination process that had changed the layered structures [29]. Fig. 3c shows $NiHPO_4$-SiO_2 surface with layered structures with relatively close distances between one pore to another. Subsequently, $Ni(H_2PO_4)_2$–SiO_2 catalyst in Fig. 3d also had layered surfaces with small aggregates dispersed on the surface, indicating the active sites of the nickel phosphate [52].

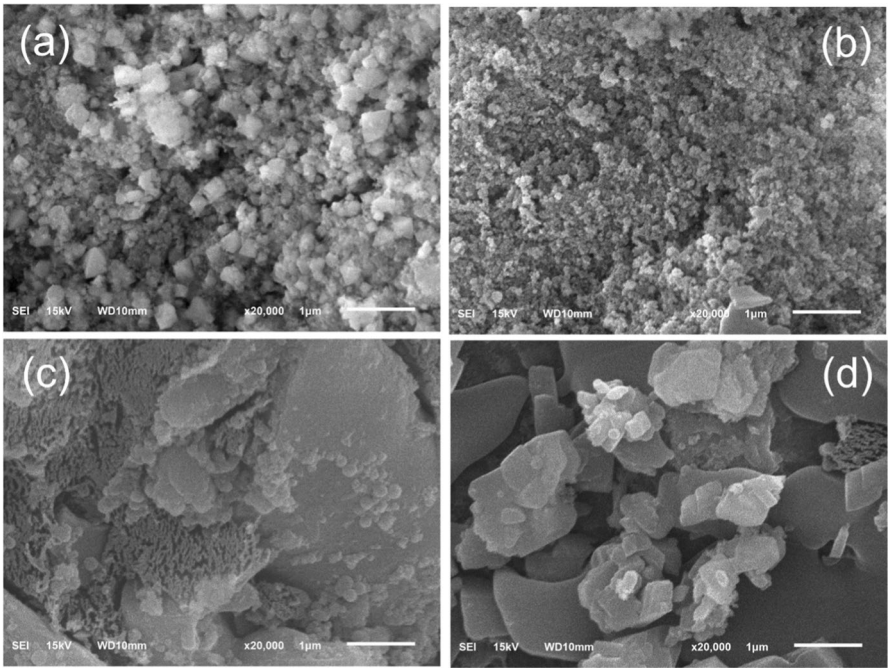

Fig. 3 SEM micrographs of **a** Ni–SiO_2, **b** $Ni_3(PO_4)_2$–SiO_2, **c** $NiHPO_4$–SiO_2 and **d** $Ni(H_2PO_4)$–SiO_2 catalysts

The EDX analysis (Supplementary Information) confirmed the existence of Si, P, O, and Ni, indicating that the nickel phosphate-silica catalysts were successfully synthesized. The P content in Ni–SiO_2 was 0% as phosphate was not incorporated onto the Ni–SiO_2 catalyst. These results also confirmed the coherency between FTIR and XRD analysis.

N_2 physisorption isotherm curves of the catalysts are presented in Fig. 4. According to the IUPAC classification, all catalysts exhibit type II adsorption isotherms [54]. Type II adsorption isotherm is associated with non-porous or macroporous solids [55]. For type II adsorption isotherm, at relatively low pressures, the volume of adsorbed gas increases sharply, indicating the incident of pore filling. Subsequently, due to completely developed macropores, the adsorption increases sharply as the P/P_o value approaches one [56]. Furthermore, at low pressures, the nearly linear point is usually associated with the monolayer adsorption and the gradual curvature, indicating conjoin of monolayer followed by the emergence of multilayer adsorption [57]. Fig. 4 also shows that all catalysts had precipitous desorption when compared to the adsorption curves. This condition is considered as hysteresis loop type B, which indicated that the catalyst had a wide distribution of pore types and diameters that usually take place in two aligned-plate cracks and slit-like pores as the major constituents [58].

The textural properties of nickel-silica phosphate derived from the N_2 physisorption isotherms are presented in Table 2. The surface area of the SiO_2 catalyst

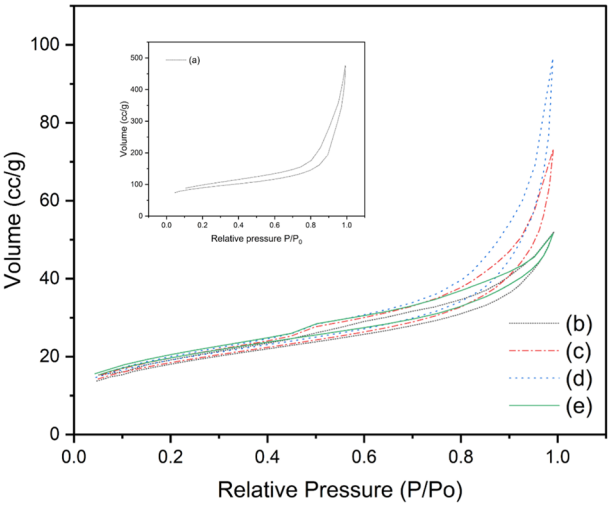

Fig. 4 N_2 adsorption–desorption isotherm curves of (a) SiO_2, (b) Ni–SiO_2, (c) $Ni_3(PO_4)_2$–SiO_2, (d) $NiHPO_4$–SiO_2 and (e) $Ni(H_2PO_4)$–SiO_2 catalysts

Table 2 Catalysts textural properties

Catalysts	BET surface area (m^2/g)	Pore volume (cm^3/g)	Pore diameter (Å)
SiO_2	280.23	0.68	97.06
Ni-SiO_2	62.77	0.08	51.23
Ni_3PO_4–SiO_2	63.76	0.11	70.89
$NiHPO_2$–SiO_2	65.74	0.16	91.27
$Ni(H_2PO_4)_2$–SiO_2	67.68	0.15	88.06

drastically decreased after being loaded by nickel and nickel phosphate species, which was probably caused by the pore's obstruction. Furthermore, it can be seen that the incorporation of phosphate ions into nickel-silica increased the surface area of catalysts from 62.77 to 63.76 m^2/g, which implied the generation of new pores by phosphate ions, thereby increasing the surface areas along with the total pore volume and pore diameter [59]. It appears that various catalysts had different surface areas depending on phosphate precursors. The highest surface area of 67.68 m^2/g was found in the $Ni(H_2PO4)_2$–SiO_2 catalyst. The high surface area prompts an increment in the number of catalytic site availability, thereby increasing the productivity of the catalyst [23]. Nonetheless, there was a reduce in the total pore volume and pore diameter of the $Ni(H_2PO_4)_2$-SiO_2 catalyst which might be due to the bulk phase partially blocking the surface pores [60].

The total acidity of the nickel-silica catalyst and nickel phosphate-silica catalysts of different precursors are shown in Table 3. The catalysts synthesized using different precursors had different total acidities. Low acidity values were observed

Table 3 Total acidity analysis of the catalysts

Catalysts	Total acidity (mmol/g)
Ni-SiO_2	0.015
Ni_3PO_4–SiO_2	0.017
$NiHPO_2$–SiO_2	0.070
$Ni(H_2PO_4)_2$–SiO_2	0.126

in Ni_3PO_4–SiO_2 and Ni–SiO_2 catalysts as both catalysts had lewis acid sites from the empty d orbitals of Ni metal that could accept a lone pair of electrons from the pyridine gas [61], and low Brønsted acid sites. Generally, the modification of nickel-silica catalyst using phosphate increases the total acidity of the catalyst. The difference in the total acidity of $Ni(H_2PO_4)_2$–SiO_2 and $NiHPO_2$–SiO_2 catalysts was not very substantial since both catalysts exhibited Brønsted acid sites from the hydrogen atoms of the phosphate groups [20], and Lewis acid sites from metal [36]. The silanol group in silica also provided another form of active site for pyridine adsorption, though not as strongly as it has a weak acid strength [62]. Remarkably, the $Ni(H_2PO_2)_2$–SiO_2 catalyst had the highest total acidity due to the high presence of Brønsted acid and Lewis acid sites [63].

Fig. 5 reveals the FTIR spectra of the catalysts after the adsorption of pyridine as indications of the Lewis and Bronsted acid sites. The FTIR spectra in Fig. 5 showed absorption bands at 1558 cm^{-1}, 1542 cm^{-1}, as well as 1508 cm^{-1}, representing the intense mode of association of the pyridine cation with the transfer of the protons from the surface OH group of the Brønsted acid sites to the corresponding molecule

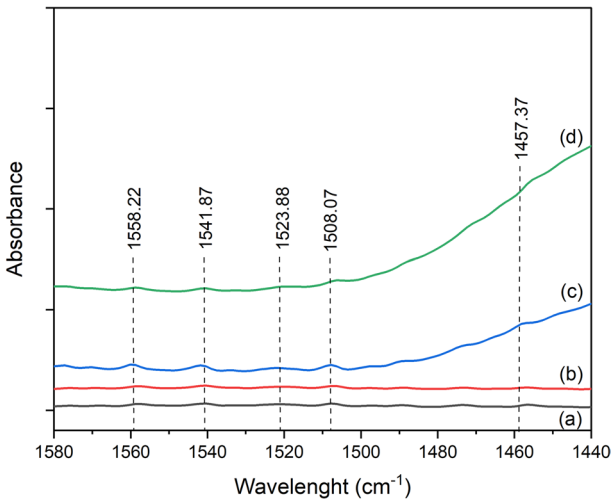

Fig. 5 FTIR spectra of (a) Ni–SiO_2, (b) $Ni_3(PO_4)_2$–SiO_2, (c) $NiHPO_4$–SiO_2 and (d) $Ni(H_2PO_4)$–SiO_2 after the adsorption of pyridine gas

[64]. According to Ni et al. [52], the absorptions are characteristic of the pyridinium ion (PhH^+), corroborating the existence of Brønsted acid site from the hydrogen in the phosphate group. The absorption peaks observed in $Ni(H_2PO_4)_2$–SiO_2 and $NiHPO_4$–SiO_2 catalysts indicated absorption through the hydrogen phosphate group. Whereas, the absorption peaks in $Ni_3(PO_4)_2$–SiO_2 and Ni–SiO_2 catalysts originated from the hydroxyl group of the Si–OH bonding. The absorption band at 1457 cm^{-1} indicated the molecularly coordinated pyridines on Ni^{2+} cations acting as Lewis acid sites [65]. Fig. 5 confirmed that $Ni(H_2PO_4)_2$–SiO_2 catalyst provided the highest absorption intensity allowing the catalyst to have the highest acidity [61]. These results are in line with the findings from the gravimetric analysis.

LA production

The production of LA from glucose was executed in a reflux system at 120 °C for 4 h, using 2 g of glucose feed and 0.5 g of catalyst in an aqueous medium. The conversion of glucose, the yield, and selectivity of LA, as well as FA, are presented in Fig. 6. It was revealed that all catalysts exhibited high conversion glucose ranging from 96.32 to 99.82%, with the LA and FA observed as a major product. The maximum glucose conversion was attained by the $Ni(H_2PO_4)_2$–SiO_2 (99.82%), whereas other catalysts showed no significant difference in the glucose conversion. As can be seen from Fig. 6, the Ni–SiO_2 catalyst produced the lowest levulinic acid yield at around 1.24%. In this catalyst, the production of LA was only aided by the metal, i.e., nickel, acting as Lewis acid active sites [66, 67]. By using $Ni_3(PO_4)_2$–SiO_2 catalyst, the levulinic acid yield was increased to 3.72%. The increase in LA yield could be attributed to the Lewis acid sites formed by metals (M) bound to the phosphate groups (M–O–P), which enhanced the catalytic activity [26, 68].

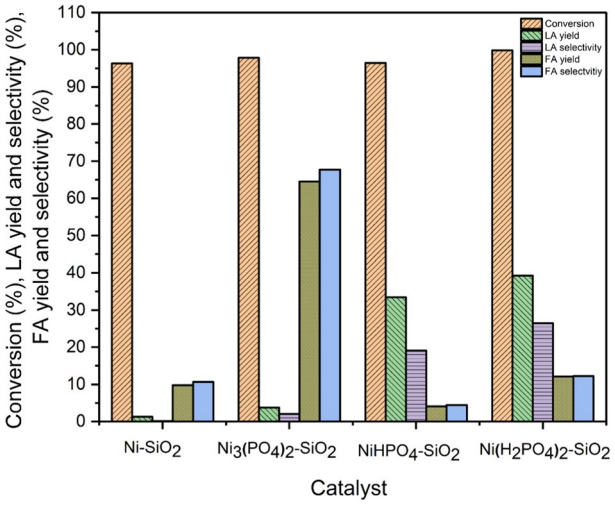

Fig. 6 Catalytic activities resulted from different catalysts (catalyst weight = 0.5 g, glucose weight = 2 g dissolved in 50 mL of DW, T = 120 °C for 3 h, stirred under reflux system)

There was a prominent increase observed in LA yield with the increment in hydrogen atoms according to the different phosphate precursors used. In general, $NiH_2(PO_4)$–SiO_2 catalyst exhibited the highest levulinic yield at 39.27%, whereas $NiHPO_4$–SiO_2 catalyst showed a 33.44% yield percentage. This increase in levulinic acid yield indicated that the hydrogen atom performed as a Brønsted acid site and played a major role in catalyzing the transformation of levulinic acid through glucose conversion. New Brønsted acid active sites were formed, generating improved catalytic activity and inherently increased the levulinic acid yield. According to Sinhamahapatra et al. [69], Brønsted acid sites mainly come from the hydrogen phosphate group. Other studies have also reported that metal phosphate catalysts provide both Lewis and Brønsted active sites [20]. Additionally, the hydrogen atom in the phosphate could form hydrogen bonds with the OH groups in glucose and strengthen the interaction among glucose and the catalyst [14]. The results showed that more hydrogen atoms were associated with more Brønsted acid active sites that, thus, would yield a higher amount of levulinic acid. Based on the acidity analysis, $NiH_2(PO_4)$–SiO_2 had the highest total acidity, indicating a positive correlation between catalyst acidity and levulinic acid yield. These findings are consistent with a previous study [12]. Similarly, the Ni–SiO_2 exhibited selectivity towards LA (0.10%), followed by the $Ni_3(PO_4)_2$–SiO_2, which only had 2.05% selectivity towards LA. The highest LA selectivity (26.49%) was achived by $Ni(H_2PO_4)_2$–SiO_2 catalyst. Weingarten et al. [20] reported that high catalyst acidity could exhibit high catalytic activity towards LA formation. Interestingly, the $Ni_3(PO_4)_2$–SiO_2 catalyst promoted high FA yield (64.53%) and selectivity, whereas the other catalysts revealed low FA formation. This condition occurred probably due to the presence of micropores, limiting the diffusion of LA molecules so that their formation was not dominant. Because FA is a smaller molecule, consequently the formation of FA is higher than LA [17]. Wei and Wu [12] reported that the catalyst 8%Cr/HZSM-5 promoted 53.7% LA yield under temperature of 180 °C for 180 min with 0.75 g catalyst. Qu et al. [14] employed the Lys-PM2 catalyst and reported that this catalyst promoted the LA yield up to 57.90% under 9 h reaction with temperature of 150 °C with glucose and catalyst ratio of 1:0.25, whereas Kumar et al. [70] reported that the 98% glucose conversion with LA yield of 63% was achieved by ionic liquid catalyst of [$C4SO_3HPhim$] [Cl] under 3 h reaction at 180 °C. This result suggests that the $Ni(H_2PO_4)_2$–SiO_2 catalyst had comparable catalytic activity towards LA production compared with other catalysts. As $Ni(H_2PO_4)_2$–SiO2 catalyst produced the highest LA yield, it was further studied and optimized using RSM-CCD. The variables observed were temperature, reaction time, and catalyst weight.

RSM-CCD analysis

RSM-CCD with three variable inputs was formulated to assess the catalytic activity of the developed catalyst. All 20 runs were performed (Table 4), and the outcomes were examined through multiple regression analysis. The coefficients were calculated and tested for their significance in view of the P-value and F-value as well.

Table 4 Experimental data of levulinic acid yield percentage

Run	Temperature (°C) Actual (coded)	Reaction time (min) Actual (coded)	Catalyst weight (g) Actual (coded)	LA yield (%)
1	110 (− 1)	120 (− 1)	0.35 (− 1)	40.34
2	130 (1)	120 (− 1)	0.35 (− 1)	25.07
3	110 (− 1)	240 (1)	0.35 (− 1)	15.54
4	130 (1)	240 (1)	0.35 (− 1)	10.31
5	110 (− 1)	120 (− 1)	0.65 (1)	30.26
6	130 (1)	120 (− 1)	0.65 (1)	34.82
7	110 (− 1)	240 (1)	0.65 (1)	30.28
8	130 (1)	240 (1)	0.65 (1)	22.29
9	103.2 (− 1.682)	180 (0)	0.5 (0)	33.44
10	136.82 (1.682)	180 (0)	0.5 (0)	35.11
11	120 (0)	79.09 (− 1.682)	0.5 (0)	42.81
12	120 (0)	280.9 (1.682)	0.5 (0)	25.50
13	120 (0)	180 (0)	0.25 (− 1.682)	23.63
14	120 (0)	180 (0)	0.75 (1.682)	23.32
15	120 (0)	180 (0)	0.5 (0)	35.67
16	120 (0)	180 (0)	0.5 (0)	35.57
17	120 (0)	180 (0)	0.5 (0)	35.48
18	120 (0)	180 (0)	0.5 (0)	35.47
19	120 (0)	180 (0)	0.5 (0)	35.66
20	120 (0)	180 (0)	0.5 (0)	35.63

The quadratic polynomial equation (in the form of coded values) from the multiple linear regression analysis is presented in the Eq. 5 as follows:

$$\begin{aligned} Y = 35.72 - 1.55A - 5.94B + 1.89C - 0.3143AB + 2.13AC \\ + 3.38BC - 1.35A^2 - 1.39B^2 - 5.17C^2 \end{aligned} \quad (5)$$

According to Eq. 2, AB, AC, AD, BC, BD, as well as CD are denoted as the interaction terms, whereas A^2, B^2, C^2, as well as D^2 are the square terms of the input variables. The positive signs in the regression coefficients indicate synergistic effects, whereas the negative signs indicate antagonistic effects on the LA yield [71].

ANOVA was performed to assess the measurable of the model significance (Table 5). The significant degree of the model and all factors (A, B, and C) was given out according to the P-value and F-value, where P-values less than 0.050 (95% confidence level) were considered significant [72]. Statistical significance could be indicated by the F-value, where a high F-value indicates that the data provided a statistically significant contribution [73]. Table 5 shows that the P-value of the model was 0.0051 and the F-value was 5.98, indicating that the model was statistically significant and represented good experimental data.

The statistical diagnostic by RSM-CCD to optimize LA yield are shown in the Supplementary Information. Internal studentized of the residues with normal

Table 5 ANOVA of response surface quadratic model for LA yield

Source	Sum of square	df	Mean square	F-value	P-value
Model	1097.97	9	122.00	5.94	0.0051
A	32.65	1	32.65	1.59	0.2359
B	482.62	1	482.62	23.51	0.0007
C	49.02	1	49.02	2.39	0.1533
AB	0.7903	1	0.7903	0.0385	0.8484
AC	36.45	1	36.45	1.78	0.2122
BC	91.41	1	91.41	4.45	0.0610
A^2	26.33	1	26.33	1.28	0.2838
B^2	28.01	1	28.01	1.36	0.2699
C^2	385.29	1	385.29	18.77	0.0015
Residual	205.30	10	20.53		
Lack of fit	205.27	5	41.05	5462.82	< 0.001
Pure error	0.0376	5	0.0075		
Cor total	1303.27	19			

probability showed that all points were close to the line, indicating no major problems with the design normality [74]. According to Tan et al. [41], normally distributed data presented in a straight line represents insignificant errors in the range of operating parameters. Random scattering data in the studentized residues versus predicted LA yield plot showed that the proposed model was adequate. These results demonstrated that the response had original variance observation, and there was no issue with the output variable [75].

Behera et al. [43] stated that if data are randomly scattered, the variation of the original observation should be constant and there is no need for a transformation of the response variable. The actual and predicted value for LA yield showed that the predicted values were consistently distributed close to the actual response. According to Garg and Jain [37], the suggested minimum value of R^2 should be 0.80 for a good model fit. In this study, the R^2 value was 0.8424, indicating that the model could evaluate up to 84.24% LA yield validated by the equation. Hence, there was a reasonable in accordance between the experimental LA yield results and the predictions from the quadratic model [40]. The outlier t plot represented the eminence residual of each run to specify which run was the individually dominant residual. According to Helmi et al. [74], the preponderance of the residuals should fall within the range + 3.879 and − 3.879 to represent operational errors in the model and actual data. In this study, the outliers from the experimental run obviously showed that all focuses in the outlier range had a good dissemination for CCD design and no data was outside this interval.

Optimization of LA yield

Fig. 7 depicts the response surface and contour plots that demonstrated the interaction effect between the two factors and LA yields. The interactions influenced by the input variables were observed to demonstrate the quadratic effect of the pertinent variable input on the LA yield. The effect of interaction between temperature and reaction time (at a constant

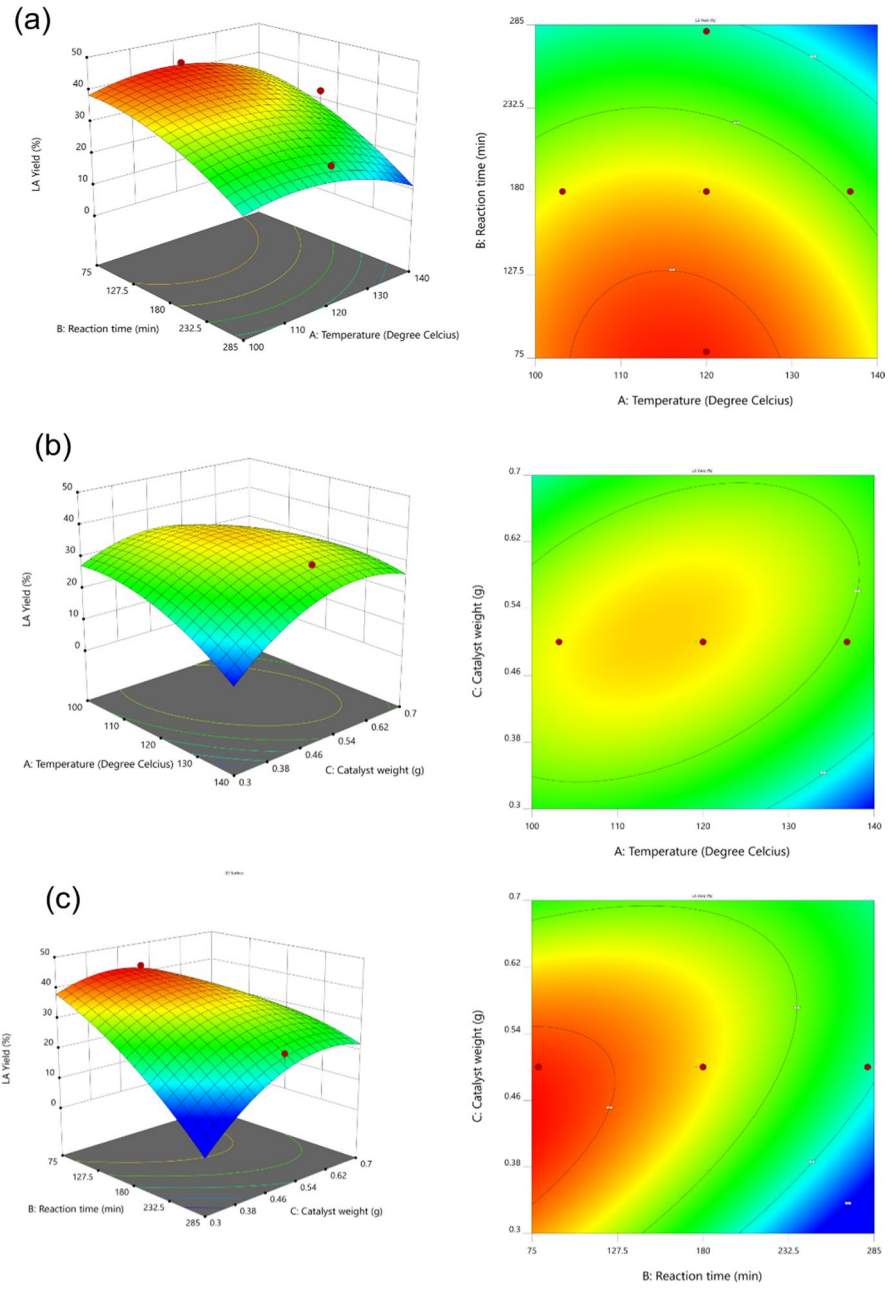

Fig. 7 3D Response fitted surface area plots and contour plots of LA yield with different variables, i.e. **a** temperature vs reaction time at a constant catalyst weight (0.5 g) **b** temperature vs catalyst weight at a constant reaction time (180 min), and **c** reaction time vs catalyst weight at a constant temperature (120 °C)

catalyst weight of 0.5 g) on LA in Fig. 7a showed that the maximum LA yield obtained was more than 40% when the temperature was in the range of 103.2–130 °C, correspondingly with a reaction time of fewer than 130 min. It can be seen from the 3D surface contour in Fig. 7a that the LA yield increased linearly with temperature and reaction time until it reached an optimum condition. This implied that an increase in temperature could cause an acceleration of the reaction rate [76]; hence under these conditions, it was very feasible for glucose to be converted into LA and for the LA yield to be increased as well. However, higher temperatures and longer reaction times allowed the side reactions to increase simultaneously, thus decreasing the LA yield. Similar findings have been reported previously [77]. From the dynamic 2D surface contour, the reaction time significantly contributed up to 30–40 of the LA yield, whereas prolonged reaction time did not increase the LA yield.

Fig. 7b appears the effect of the interaction between the catalyst weight and the reaction temperature (at a constant reaction time of 180 min) on LA yield. Through this interaction, a maximum LA yield of more than 35% was obtained at a temperature between 106 and 125 °C and a catalyst weight between 0.44 and 0.58 g. The LA yield increased with increasing catalyst weight. This is associated with more available active sites in the reaction system, thus increasing LA yield [78]. According to Dharne and Bokade [5], the increase in LA yield attributed to the increasing amount of catalyst loading is also due to the availability of a large surface area, which favors the dispersion of the active species. Therefore, the accessibility of reactant molecules at the active site of the catalyst is preferable. A further increase in catalyst weight was negatively correlated with LA yields, presumably due to the mass transfer resistance of the catalyst [79]. After the catalyst weight met the ideal necessities, a prolonged reaction temperature resulted in a lower LA yield. In this condition, by-products such as formic acid were likely more dominant, thereby reducing the LA yield. Furthermore, it was feasible to realize that reactive compounds resulting from the glucose conversion presumably collided with 5-HMF and caused cross-polymerization to produce undesired products [80]. The highly dynamic interactions between A and C were seen in the 3D surface plots showing the effectiveness of the catalyst performance in this study in the low-temperature range.

Moreover, Fig. 7c appears that the maximum LA yield was obtained by more than 40% when the reaction time was less than 125 min and catalyst weight was 0.34–0.55 g (at a constant temperature of 120 min). As illustrated in Fig. 7c, at a certain point, an increase in either of these two variables did not result in a prominent response of LA yield. A further increase in the amount of catalyst did not show a significant increase in the LA yield, which might be ascribed to the emergence of a by-product called humin being predominant. The formation of humin may be responsible for the condensation reactions of glucose, fructose, and 5-HMF [70]. After 125 min, it was found that the active center of the catalyst could be covered by humin and other polymeric compounds that reduce LA yield [81]. Similar findings were reported by Ramli and Amin [82] previously.

Process variables were optimized using RSM-CCD based on LA yield and compared with experimental results. Optimum process parameters were predicted at the temperature of 113.20 °C, the reaction time of 120 min, and the catalyst weight of 0.4573 g. The LA yield for this optimum processing parameter was estimated at 40.89%. The desirability of the applied model was 94% for this predictive value. Experiments were conducted and it was found that the predicted LA yield was close

Table 6 Reusability performance of $Ni(H_2PO_4)_2$–SiO_2 catalyst for LA fornation

Run	LA yield (%)
1st	40.70
2nd	40.25
3rd	39.43
4th	36.53
5th	34.46

to the experimental value, which had an error below ± 5%. This proved the RSM-CCD design is a great tool to specify optimum conditions. The stable process performance can be ascribed to the synthesized of nickel phosphate-silica with suitable physicochemical properties, good interaction between all the selected factors, and preferable experimental design.

As presented in Table 6, the reusability performance of the $Ni(H_2PO_4)_2$–SiO_2 catalyst on the glucose conversion and LA yield was evaluated at 5 consecutive runs under optimized conditions. It can be seen that at 2 consecutive reactions, the catalytic activity of the catalyst only decreased by 1.15% compared with the first catalyst tests. Afterward, the catalytic activity tended to decrease up to 3.12% at 3 consecutive runs and gradually decreased at 5 consecutive runs. The decrease in LA yield was presumably due to the loss of active catalytic sites during the multiple cleaning steps [82]. However, this catalyst was still active at 5 consecutive runs with a slight decrease toward LA formation.

Conclusions

Nickel phosphate-silica catalyst had been synthesized with different phosphate precursors and used to convert glucose into levulinic acid. Catalyst characterization showed that the phosphate ion had been successfully incorporated onto nickel-silica catalyst and increased the acidity of the catalyst. The present study showed that catalytic activity increased significantly with increased in hydrogen atoms from the different phosphate precursors. $Ni(H_2PO_4)_2$–SiO_2 catalyst exhibited the highest catalytic activity and surface area compared to other catalysts. Furthermore, the optimum levulinic acid production using $Ni(H_2PO_4)_2$–SiO_2 catalyst by RSM-CCD was achieved at a temperature of 113.20 °C, a reaction time of 120 min, and a catalyst weight of 0.4573 g, with LA yield of 40.89%. The obtained model was statistically significant with good adequate precision. Overall, the results of this work can provide preliminary report regarding the potential of nickel phosphate-silica catalysts for the production of levulinic acid as high-value products.

Supplementary Information The online version contains supplementary material available at https://doi.org/10.1007/s11144-022-02334-3.

Acknowledgements Authors thank Biofuel Research Group, Biofuel Research Group, Laboratory of Physical Chemistry, Faculty of Mathematics and Natural Science, Universitas Sriwijaya for providing research resources.

Declarations

Conflict of interest The authors have no competing interests to declare that are relevant to the content of this article.

References

1. Fanani Z, Hasanudin H, Rachmat A, Said M (2021) Comparison of Cr/C and Cr_2O_3/Z catalysts on hydrocracking of bio-oil from pyrolysis of palm empty fruit bunches. Molekul 16:244–252. https://doi.org/10.20884/1.jm.2021.16.3.812
2. Galadima A, Muraza O (2020) Waste materials for production of biodiesel catalysts: Technological status and prospects. J Clean Prod 263:121358. https://doi.org/10.1016/j.jclepro.2020.121358
3. Sari EP, Wijaya K, Trisunaryanti W, Syoufian A, Hasanudin H, Saputri WD (2022) The effective combination of zirconia superacid and zirconia-impregnated CaO in biodiesel manufacturing: utilization of used coconut cooking oil (UCCO). Int J Energy Environ Eng 13:967–978. https://doi.org/10.1007/s40095-021-00439-4
4. Jeong GT, Kim SK (2021) Methanesulfonic acid-mediated conversion of microalgae Scenedesmus obliquus biomass into levulinic acid. J Ind Eng Chem 104:85–92. https://doi.org/10.1016/j.jiec.2021.08.013
5. Dharne S, Bokade VV (2011) Esterification of levulinic acid to n-butyl levulinate over heteropolyacid supported on acid-treated clay. J Nat Gas Chem 20:18–24. https://doi.org/10.1016/S1003-9953(10)60147-8
6. Pyo SH, Glaser SJ, Rehnberg N, Hatti-Kaul R (2020) Clean production of levulinic acid from fructose and glucose in salt water by heterogeneous catalytic dehydration. ACS Omega 5:14275–14282. https://doi.org/10.1021/acsomega.9b04406
7. Signoretto M, Taghavi S, Ghedini E, Menegazzo F (2019) Catalytic production of levulinic acid (LA) from actual biomass. Molecules 24:1–20. https://doi.org/10.3390/molecules24152760
8. Moustani C, Anagnostopoulou E, Krommyda K, Moustani C, Anagnostopoulou E, Krommyda K, Panopoulou C, Koukoulakis KG, Bakeas EB, Papadogianakis G (2018) Novel aqueous-phase hydrogenation reaction of the key biorefinery platform chemical levulinic acid into γ-valerolactone employing highly active, selective and stable water-soluble ruthenium catalysts modified with nitrogen-containing ligands. Appl Catal B Environ 238:82–92. https://doi.org/10.1016/j.apcatb.2018.07.009
9. Kang S, Fu J, Zhang G (2018) From lignocellulosic biomass to levulinic acid: a review on acid-catalyzed hydrolysis. Renew Sustain Energy Rev 94:340–362. https://doi.org/10.1016/j.rser.2018.06.016
10. Badgujar KC, Badgujar VC, Bhanage BM (2020) A review on catalytic synthesis of energy rich fuel additive levulinate compounds from biomass derived levulinic acid. Fuel Process Technol 197:106213. https://doi.org/10.1016/j.fuproc.2019.106213
11. Ranoux A, Djanashvili K, Arends IWCE, Hanefeld U (2013) 5-Hydroxymethylfurfural synthesis from hexoses is autocatalytic. ACS Catal 3:760–763. https://doi.org/10.1021/cs400099a
12. Wei W, Wu S (2018) Experimental and kinetic study of glucose conversion to levulinic acid in aqueous medium over Cr/HZSM-5 catalyst. Fuel 225:311–321. https://doi.org/10.1016/j.fuel.2018.03.120
13. Liu B, Ba C, Jin M, Zhang Z (2015) Effective conversion of carbohydrates into biofuel precursor 5-hydroxymethylfurfural (HMF) over Cr-incorporated mesoporous zirconium phosphate. Ind Crops Prod 76:781–786. https://doi.org/10.1016/j.indcrop.2015.07.036
14. Qu H, Liu B, Gao G, Ma Y, Zhou Y, Zhou H, Li L, Li Y, Liu S (2019) Metal-organic framework containing Br Ønsted acidity and Lewis acidity for efficient conversion glucose to levulinic acid. Fuel Process Technol 193:1–6. https://doi.org/10.1016/j.fuproc.2019.04.035

15. Mongkolpichayarak I, Jiraroj D, Anutrasakda W, Ngamcharussrivichai C, Samec JSM, Tungasmita DN (2021) Cr/MCM-22 catalyst for the synthesis of levulinic acid from green hydrothermolysis of renewable biomass resources. J Catal 405:373–384. https://doi.org/10.1016/j.jcat.2021.12.019
16. Zhuang JP, Li XP, Liu Y (2012) Conversion of glucose to levulinic acid using SO_4^{2-}/TiO_2-Al_2O_3-SnO_2 solid acid catalysts. Adv Mater Res 550–553:234–237. https://doi.org/10.4028/www.scientific.net/AMR.550-553.234
17. Zeng W, Cheng DG, Zhang H, Chen F, Zhan X (2010) Dehydration of glucose to levulinic acid over MFI-type zeolite in subcritical water at moderate conditions. React Kinet Mech Catal 100:377–384. https://doi.org/10.1007/s11144-010-0187-x
18. Guzmán I, Heras A, Güemez MB, Iriondo A, Cambra JF, Requies J (2016) Levulinic acid production using solid-acid catalysis. Ind Eng Chem Res 55:5139–5144. https://doi.org/10.1021/acs.iecr.5b04190
19. Zeng W, Cheng DG, Chen F, Zhan X (2009) Catalytic conversion of glucose on Al–Zr mixed oxides in hot compressed water. Catal Letters 133:221–226. https://doi.org/10.1007/s10562-009-0160-3
20. Weingarten R, Kim YT, Tompsett GA, Fernández A, Han KS, Hagaman EW, Conner WC, Dumesic JA, Huber GW (2013) Conversion of glucose into levulinic acid with solid metal(IV) phosphate catalysts. J Catal 304:123–134. https://doi.org/10.1016/j.jcat.2013.03.023
21. Bej B, Pradhan NC, Neogi S (2013) Production of hydrogen by steam reforming of methane over alumina supported nano-NiO/SiO_2 catalyst. Catal Today 207:28–35. https://doi.org/10.1016/j.cattod.2012.04.011
22. Mallesham B, Sudarsanam P, Reddy BVS, Rao BG, Reddy BM (2018) Nanostructured nickel/silica catalysts for continuous flow conversion of levulinic acid to γ-valerolactone. ACS Omega 3:16839–16849. https://doi.org/10.1021/acsomega.8b02008
23. Ye RP, Gong W, Sun Z, Sheng Q, Shi X, Wang T, Yao Y, Razink JJ, Lin L, Zhou Z, Adidharma H, Tang J, Fan M, Yao YG (2019) Enhanced stability of Ni/SiO_2 catalyst for CO_2 methanation: derived from nickel phyllosilicate with strong metal-support interactions. Energy 188:116059. https://doi.org/10.1016/j.energy.2019.116059
24. Tang Y, Liu Z, Guo W, Chen T, Qiao Y, Mu S, Zhao Y, Gao F (2016) Honeycomb-like mesoporous cobalt nickel phosphate nanospheres as novel materials for high performance supercapacitor. Electrochim Acta 190:118–125. https://doi.org/10.1016/j.electacta.2016.01.042
25. Sharma P, Radhakrishnan S, Khil MS, Kim HY, Kim BS (2018) Simple room temperature synthesis of porous nickel phosphate foams for electrocatalytic ethanol oxidation. J Electroanal Chem 808:236–244. https://doi.org/10.1016/j.jelechem.2017.12.025
26. Ordomsky VV, Sushkevich VL, Schouten JC, Van Der Schaaf J, Nijhuis TA (2013) Glucose dehydration to 5-hydroxymethylfurfural over phosphate catalysts. J Catal 300:37–46. https://doi.org/10.1016/j.jcat.2012.12.028
27. Sun X, Wang J, Yin Y, Wang H, Li S, Liu H, Ma J, Du X (2020) Laser-Ablation-produced cobalt nickel phosphate with high-valence nickel ions as an active catalyst for the oxygen evolution reaction. Chem A Eur J 26:2793–2797. https://doi.org/10.1002/chem.201904510
28. Li Y, Zhao C (2016) Iron-doped nickel phosphate as synergistic electrocatalyst for water oxidation. Chem Mater 28:5659–5666. https://doi.org/10.1021/acs.chemmater.6b01522
29. Omar FS, Numan A, Duraisamy N, Bashir S, Ramesh K, Ramesh S (2016) Ultrahigh capacitance of amorphous nickel phosphate for asymmetric supercapacitor applications. RSC Adv 6:76298–76306. https://doi.org/10.1039/c6ra15111f
30. Liu H, Haoyi L, Wang X (2016) Electrostatic Interaction-directed growth of nickel phosphate single-walled nanotubes for high performance oxygen evolution reaction catalysts. Small 12:2969–2974. https://doi.org/10.1002/smll.201600345
31. Chong R, Wang B, Li D, Chang Z, Zhang L (2017) Enhanced photoelectrochemical activity of Nickel-phosphate decorated phosphate-Fe_2O_3 photoanode for glycerol-based fuel cell. Sol Energy Mater Sol Cells 160:287–293. https://doi.org/10.1016/j.solmat.2016.10.052
32. Limlamthong M, Chitpong N, Jongsomjit B (2019) Influence of phosphoric acid modification on catalytic properties of Al2O3 catalysts for dehydration of ethanol to diethyl ether. Bull Chem React Eng Catal 14:1–8. https://doi.org/10.9767/bcrec.14.1.2436.1-8
33. Song X, Gao L, Li Y, Chen W, Mao L, Yang JH (2017) Nickel phosphate-based materials with excellent durability for urea electro-oxidation. Electrochim Acta 251:284–292. https://doi.org/10.1016/j.electacta.2017.08.117

34. Hasanudin H, Asri WR, Tampubolon K, Riyant F, Purwaningrum W, Wijaya K (2022) Dehydration isopropyl alcohol to diisopropyl ether over molybdenum phosphide pillared bentonite. Pertanika J Sci Technol 30:1739–1754. https://doi.org/10.47836/pjst.30.2.47
35. Samuel OD, Okwu MO, Oyejide OJ, Taghinezhad E, Afzal A, Kaveh M (2020) Optimizing biodiesel production from abundant waste oils through empirical method and grey wolf optimizer. Fuel 281:118701. https://doi.org/10.1016/j.fuel.2020.118701
36. Hasanudin H, Asri WR, Said M, Hidayati PT, Purwaningrum W, Novia N, Wijaya K (2022) Hydrocracking optimization of palm oil to bio-gasoline and bio-aviation fuels using molybdenum nitride-bentonite catalyst. RSC Adv 12:16431–16443. https://doi.org/10.1039/D2RA02438A
37. Garg A, Jain S (2020) Process parameter optimization of biodiesel production from algal oil by response surface methodology and artificial neural networks. Fuel 277:118254. https://doi.org/10.1016/j.fuel.2020.118254
38. Yahya S, Muhamad Wahab SK, Harun FW (2020) Optimization of biodiesel production from waste cooking oil using Fe-Montmorillonite K10 by response surface methodology. Renew Energy 157:164–172. https://doi.org/10.1016/j.renene.2020.04.149
39. Al-Sakkari EG, Abdeldayem OM, El-Sheltawy ST, Abadir MF, Soliman A, Rene ER, Ismail I (2020) Esterification of high FFA content waste cooking oil through different techniques including the utilization of cement kiln dust as a heterogeneous catalyst: A comparative study. Fuel 279:118519. https://doi.org/10.1016/j.fuel.2020.118519
40. Qu T, Niu S, Gong Z, Han K, Wang Y, Lu C (2020) Wollastonite decorated with calcium oxide as heterogeneous transesterification catalyst for biodiesel production: optimized by response surface methodology. Renew Energy 159:873–884. https://doi.org/10.1016/j.renene.2020.06.009
41. Tan YH, Abdullah MO, Nolasco-Hipolito C, Ahmad Zauzi NS (2017) Application of RSM and Taguchi methods for optimizing the transesterification of waste cooking oil catalyzed by solid ostrich and chicken-eggshell derived CaO. Renew Energy 114:437–447. https://doi.org/10.1016/j.renene.2017.07.024
42. Hasanudin H, Putri QU, Agustina TE, Hadiah F (2022) Esterification of free fatty acid in palm oil mill effluent using sulfated carbon-zeolite composite catalyst. Pertanika J Sci Technol 30:377–395. https://doi.org/10.47836/pjst.30.1.21
43. Behera SK, Meena H, Chakraborty S, Meikap BC (2018) Application of response surface methodology (RSM) for optimization of leaching parameters for ash reduction from low-grade coal. Int J Min Sci Technol 28:621–629. https://doi.org/10.1016/j.ijmst.2018.04.014
44. Rioux RM, Song H, Hoefelmeyer JD, Yang P, Somorjai GA (2005) High-surface-area catalyst design: synthesis, characterization, and reaction studies of platinum nanoparticles in mesoporous SBA-15 silica. J Phys Chem B 109:2192–2202. https://doi.org/10.1021/jp048867x
45. Chen X, Jin J, Sha G, Li C, Zhang B, Su D, Williams CT, Liang C (2014) Silicon-nickel intermetallic compounds supported on silica as a highly efficient catalyst for CO methanation. Catal Sci Technol 4:53–61. https://doi.org/10.1039/c3cy00743j
46. Ergul E, Kurt HI, Oduncuoglu M (2020) Electroless nickel-phosphorus and cobalt-phosphorus coatings on multi-walled carbon nanotubes. Mater Res Express 7:115604. https://doi.org/10.1088/2053-1591/abcc3f
47. Praseptiangga D, Zahara HL, Widjanarko PI, Joni IM, Panatarani C (2020) Preparation and FTIR spectroscopic studies of SiO_2–ZnO nanoparticles suspension for the development of carrageenan-based bio-nanocomposite film. AIP Conf Proc 2219:100005. https://doi.org/10.1063/5.0003434
48. Malinowski S, Tyblewski M (1979) Properties and catalytic activity of nickel phosphate catalyst. J Colloid Interface Sci 71:560–569. https://doi.org/10.1016/0021-9797(79)90329-1
49. Kullyakool S, Danvirutai C, Siriwong K, Noisong P (2014) Determination of kinetic triplet of the synthesized $Ni_3(PO_4)_2{\cdot}8H_2O$ by non-isothermal and isothermal kinetic methods. J Therm Anal Calorim 115:1497–1507. https://doi.org/10.1007/s10973-013-3399-2
50. Al-Omair MA, Touny AH, Saleh MM (2017) Reflux-based synthesis and electrocatalytic characteristics of nickel phosphate nanoparticles. J Power Sour 342:1032–1039. https://doi.org/10.1016/j.jpowsour.2016.09.079
51. Ermakova MA, Ermakov DY (2003) High-loaded nickel-silica catalysts for hydrogenation, prepared by sol-gel: route—structure and catalytic behavior. Appl Catal A Gen 245:277–288. https://doi.org/10.1016/S0926-860X(02)00648-8
52. Ni W, Li D, Zhao X, Ma W, Kong K, Gu Q, Chen M, Hou Z (2019) Catalytic dehydration of sorbitol and fructose by acid-modified zirconium phosphate. Catal Today 319:66–75. https://doi.org/10.1016/j.cattod.2018.03.034

53. Majewski AJ, Wood J, Bujalski W (2013) Nickel-silica core@shell catalyst for methane reforming. Int J Hydrogen Energy 38:14531–14541. https://doi.org/10.1016/j.ijhydene.2013.09.017
54. Sing KSW, Williams RT (2004) Physisorption hysteresis loops and the characterization of nanoporous materials. Adsorpt Sci Technol 22:773–782. https://doi.org/10.1260/0263617053499032
55. Cychosz KA, Thommes M (2018) Progress in the physisorption characterization of nanoporous gas storage materials. Engineering 4:559–566. https://doi.org/10.1016/j.eng.2018.06.001
56. Zhang Y, Shao D, Yan J, Jia X, Li Y, Yu P, Zhang T (2016) The pore size distribution and its relationship with shale gas capacity in organic-rich mudstone of Wufeng-Longmaxi formations, Sichuan Basin, China. J Nat Gas Geosci 1:213–220. https://doi.org/10.1016/j.jnggs.2016.08.002
57. Thommes M, Kaneko K, Neimark AV, Olivier JP, Rodriguez-Reinoso F, Rouquerol J, Sing KSW (2015) Physisorption of gases, with special reference to the evaluation of surface area and pore size distribution (IUPAC Technical Report). Pure Appl Chem 87:1051–1069. https://doi.org/10.1515/pac-2014-1117
58. Labani MM, Rezaee R, Saeedi A, Al HA (2013) Evaluation of pore size spectrum of gas shale reservoirs using low pressure nitrogen adsorption, gas expansion and mercury porosimetry: A case study from the Perth and Canning Basins, Western Australia. J Pet Sci Eng 112:7–16. https://doi.org/10.1016/j.petrol.2013.11.022
59. Yaripour F, Baghaei F, Schmidt I, Perregaarad J (2005) Synthesis of dimethyl ether from methanol over aluminium phosphate and silica-titania catalysts. Catal Commun 6:542–549. https://doi.org/10.1016/j.catcom.2005.05.003
60. González-castaño M, Le SE, Berry C, Pastor-pérez L, Arellano-garcía H, Wang Q, Reina TR (2021) Nickel phosphide catalysts as efficient systems for CO_2 upgrading via dry reforming of methane. Catalysts 11:1–11. https://doi.org/10.3390/catal11040446
61. Wijaya K, Malau LLM, Utami M, Mulijani S, Patah A, Wibowo AC, Chandrasekaran M, Rajabathar JR, Al-Lohedan HA (2021) Synthesis, characterizations and catalysis of sulfated silica and nickel modified silica catalysts for diethyl ether (DEE) production from ethanol towards renewable energy applications. Catalysts 11:1511. https://doi.org/10.3390/catal11121511
62. Busca G (2019) Catalytic materials based on silica and alumina: Structural features and generation of surface acidity. Prog Mater Sci 104:215–249. https://doi.org/10.1016/j.pmatsci.2019.04.003
63. Hauli L, Wijaya K, Armunanto R (2018) Preparation and characterization of sulfated zirconia from a commercial zirconia nanopowder. Orient J Chem 34:1559–1564. https://doi.org/10.13005/ojc/340348
64. Zaccheria F, Santoro F, Iftitah ED, Ravasio N (2018) Brønsted and lewis solid acid catalysts in the valorization of citronellal. Catalysts 8:410. https://doi.org/10.3390/catal8100410
65. Reddy CR, Bhat YS, Nagendrappa G, Jai Prakash BS (2009) Brønsted and Lewis acidity of modified montmorillonite clay catalysts determined by FT-IR spectroscopy. Catal Today 141:157–160. https://doi.org/10.1016/j.cattod.2008.04.004
66. Marianou AA, Michailof CM, Pineda A, Iliopoulou EF, Triantafyllidis KS, Lappas AA (2018) Effect of Lewis and Br Ønsted acidity on glucose conversion to 5-HMF and lactic acid in aqueous and organic media. Appl Catal A Gen 555:75–87. https://doi.org/10.1016/j.apcata.2018.01.029
67. Jiang L, Zhou L, Chao J, Zhao H, Lu T, Su Y, Yang X, Xu J (2018) Direct catalytic conversion of carbohydrates to methyl levulinate: synergy of solid Br Ønsted acid and Lewis acid. Appl Catal B Environ 220:589–596. https://doi.org/10.1016/j.apcatb.2017.08.072
68. Hasanudin H, Asri WR, Zulaikha IS, Ayu C, Rachmat A, Riyanti F, Hadiah F, Zainul R, Maryana R (2022) Hydrocracking of crude palm oil to a biofuel using zirconium nitride and zirconium phosphide-modified bentonite. RSC Adv 12:21916–21925. https://doi.org/10.1039/d2ra03941a
69. Sinhamahapatra A, Sutradhar N, Roy B, Tarafdar A, Bajaj HC, Panda AB (2010) Mesoporous zirconium phosphate catalyzed reactions: Synthesis of industrially important chemicals in solvent-free conditions. Appl Catal A Gen 385:22–30. https://doi.org/10.1016/j.apcata.2010.06.016
70. Kumar K, Kumar M, Upadhyayula S (2021) Catalytic conversion of glucose into levulinic acid using 2-phenyl-2-imidazoline based ionic liquid catalyst. Molecules. https://doi.org/10.3390/molecules26020348
71. Shahedi M, Habibi Z, Yousefi M, Mohammadi M, Brask J (2021) Improvement of biodiesel production from palm oil by co-immobilization of *Thermomyces lanuginosa* lipase and Candida antarctica lipase B: optimization using response surface methodology. Int J Biol Macromol 170:490–502. https://doi.org/10.1016/j.ijbiomac.2020.12.181

72. Said M, Ba-Abbad MM, Abdullah SRS, Mohammad AW (2017) Application of response surface method in reverse osmosis membrane to optimize BOD, COD and colour removal from palm oil mill effluent. Int J Adv Sci Eng Inf Technol 7:1871–1878. https://doi.org/10.18517/ijaseit.7.5.1844
73. Narula V, Khan MF, Negi A, Kalra S, Thakur A, Jain S (2017) Low temperature optimization of biodiesel production from algal oil using CaO and CaO/Al_2O_3 as catalyst by the application of response surface methodology. Energy 140:879–884. https://doi.org/10.1016/j.energy.2017.09.028
74. Helmi M, Tahvildari K, Hemmati A, Aberoomand azar P, Safekordi A, (2020) Phosphomolybdic acid/graphene oxide as novel green catalyst using for biodiesel production from waste cooking oil via electrolysis method: Optimization using with response surface methodology (RSM). Fuel 287:119528. https://doi.org/10.1016/j.fuel.2020.119528
75. Pooja S, Anbarasan B, Ponnusami V, Arumugam A (2021) Efficient production and optimization of biodiesel from kapok (Ceiba pentandra) oil by lipase transesterification process: addressing positive environmental impact. Renew Energy 165:619–631. https://doi.org/10.1016/j.renene.2020.11.053
76. Sharma M, Toor AP, Wanchoo RK (2014) Reaction kinetics of catalytic esterification of nonanoic acid with ethanol over amberlyst 15. Int J Chem React Eng 12:451–463. https://doi.org/10.1515/ijcre-2014-0068
77. Peng L, Lin L, Zhang J, Zhuang J, Zhang B, Gong Y (2010) Catalytic conversion of cellulose to levulinic acid by metal chlorides. Molecules 15:5258–5272. https://doi.org/10.3390/molecules15085258
78. Ramli NAS, Amin NAS (2015) Optimization of oil palm fronds conversion to levulinic acid using Fe/HY zeolite catalyst. Sains Malaysiana 44:883–890. https://doi.org/10.17576/jsm-2015-4406-15
79. Booramurthy VK, Kasimani R, Subramanian D, Pandian S (2020) Production of biodiesel from tannery waste using a stable and recyclable nano-catalyst: An optimization and kinetic study. Fuel 260:116373. https://doi.org/10.1016/j.fuel.2019.116373
80. Ramli NAS, Amin NAS (2017) Optimization of biomass conversion to levulinic acid in acidic ionic liquid and upgrading of levulinic acid to ethyl levulinate. Bioenergy Res 10:50–63. https://doi.org/10.1007/s12155-016-9778-3
81. Bokade V, Moondra H, Niphadkar P (2020) Highly active Brønsted acidic silicon phosphate catalyst for direct conversion of glucose to levulinic acid in MIBK–water biphasic system. SN Appl Sci. https://doi.org/10.1007/s42452-019-1827-z
82. Ramli NAS, Amin NAS (2015) Optimization of renewable levulinic acid production from glucose conversion catalyzed by Fe/HY zeolite catalyst in aqueous medium. Energy Convers Manag 95:10–19. https://doi.org/10.1016/j.enconman.2015.02.013

Authors and Affiliations

Qodria Utami Putri[1,2] · Hasanudin Hasanudin[2,3] · Wan Ryan Asri[1,2] · Ady Mara[2,3] · Roni Maryana[4] · Saharman Gea[5] · Karna Wijaya[6]

[1] Magister Program, Department of Chemistry, Faculty of Mathematics and Natural Science, Universitas Sriwijaya, Indralaya 30662, Indonesia

[2] Department of Chemistry, Faculty of Mathematics and Natural Science, Universitas Sriwijaya, Indralaya 30662, Indonesia

[3] Laboratory of Physical Chemistry, Biofuel Research Group, Faculty of Mathematics and Natural Science, Universitas Sriwijaya, Indralaya 30662, Indonesia

[4] Research Center for Chemistry, National Research and Innovation Agency (BRIN-Indonesia), Science and Technology Park B.J. Habibie, Serpong, South Tangerang, 15314, Indonesia

[5] Department of Chemistry, Faculty of Mathematics and Natural Science, University of Sumatra Utara, Medan 20155, Indonesia

[6] Department of Chemistry, Faculty of Mathematics and Natural Science, Universitas Gadjah Mada, Yogyakarta 55281, Indonesia